Clim. Past, 20, 25–36, 2024
https://doi.org/10.5194/cp-20-25-2024

Climate of the Past
Open Access
EGU

Nonlinear increase in seawater $^{87}Sr / ^{86}Sr$ in the Oligocene to early Miocene and implications for climate-sensitive weathering

Heather M. Stoll[1], Leopoldo D. Pena[2], Ivan Hernandez-Almeida[1], José Guitián[1,a], Thomas Tanner[1], and Heiko Pälike[3]

[1]Department of Earth Science, ETH Zurich, Zurich, 8092, Switzerland
[2]GRC Geociències Marines, Dept. Dinàmica de la Terra i de l'Oceà, Facultat de Ciències de la Terra, Universitat de Barcelona, Barcelona, 28080, Spain
[3]MARUM Centre for Marine Environmental Sciences, University of Bremen, 28359 Bremen, Germany
[a]present address: Centro de Investigación Mariña, Universidade de Vigo, GEOMA, Vigo, 36310, Spain

Correspondence: Heather M. Stoll (heather.stoll@erdw.ethz.ch)

Received: 23 April 2023 – Discussion started: 23 May 2023
Revised: 8 October 2023 – Accepted: 23 October 2023 – Published: 3 January 2024

Abstract. The $^{87}Sr / ^{86}Sr$ of marine carbonates provides a key constraint on the balance of continental weathering and hydrothermal Sr fluxes to the ocean, and the mid-Oligocene to mid-Miocene period features the most rapid rates of increase in the $^{87}Sr / ^{86}Sr$ of the Cenozoic. Because previous records of the $^{87}Sr / ^{86}Sr$ increase with time were based on biostratigraphically defined age models in diverse locations, it was difficult to unambiguously distinguish million-year-scale variations in the rate of $^{87}Sr / ^{86}Sr$ change from variations in sedimentation rate. In this study, we produce the first $^{87}Sr / ^{86}Sr$ results from an Oligocene to early Miocene site with a precise age-model-derived orbital tuning of high-resolution benthic $\delta^{18}O$ at Equatorial Pacific Ocean Drilling Program (ODP) Site 1218. Our new dataset resolves transient decreases in $^{87}Sr / ^{86}Sr$, as well as periods of relative stasis. These changes can be directly compared with the high-resolution benthic $\delta^{18}O$ at the same site. We find that slowing of the rate of $^{87}Sr / ^{86}Sr$ increase coincides with the onset of Antarctic ice expansion at the beginning of the mid-Oligocene glacial interval, and a rapid steeping in the $^{87}Sr / ^{86}Sr$ increase coincides with the benthic $\delta^{18}O$ evidence for rapid ice retreat. This pattern may reflect either northward shifts in the Intertropical Convergence Zone precipitation to areas of nonradiogenic bedrock and/or lowered weathering fluxes from highly radiogenic glacial flours on Antarctica. We additionally generate the first $^{87}Sr / ^{86}Sr$ data from ODP Site 1168 on the Tasman Rise and Integrated Ocean Drilling Program (IODP) Site 1406 of the Newfoundland Margin during the Oligocene to early Miocene to improve the precision of age correlation of these Northern Hemisphere and Southern Hemisphere midlatitude sites and to better estimate the duration of early Miocene hiatus and condensed sedimentation.

1 Introduction

The mid-Oligocene through the mid-Miocene period features the fastest rate of change in seawater $^{87}Sr / ^{86}Sr$ of the Cenozoic, evidence of significant change in the balance of Sr sources to the ocean. Although the precise causes of the Cenozoic $^{87}Sr / ^{86}Sr$ change remain under discussion, to first order the rise reflects an increase in the supply of dissolved Sr sourced from weathering of older rocks of higher $^{87}Sr / ^{86}Sr$, which are found on continents, compared to the supply of dissolved Sr from rocks of lower $^{87}Sr / ^{86}Sr$ characterizing submarine volcanic weathering and subaerial weathering of young volcanic provinces (Palmer and Elderfield, 1985). This change in balance of sources can be accomplished by one or more processes including a decrease in the rate of hydrothermal weathering, an increase in total continental weathering, or changes in the $^{87}Sr / ^{86}Sr$ of continental weathering flux due to either changes in the location of the most intense weathering or changes in the composition and average age (Peucker-Ehrenbrink and Fiske, 2019) of rocks exposed to weathering.

The Oligocene–early Miocene is a period of very rapid increase in $^{87}Sr / ^{86}Sr$, with multiple possible drivers includ-

ing the unroofing of highly radiogenic source rocks in the Himalaya (Galy et al., 1996; Yang et al., 2022; Myrow et al., 2015). Within the Oligocene–early Miocene period of rapid increase in $^{87}Sr/^{86}Sr$, some previous studies have suggested the potential for 1–3-million-year timescale variations in the rate of increase (Oslick et al., 1994) and proposed that the liberation of Sr from silicate weathering may respond to changes in the production and exposure of glacially floured rock on Antarctica (Miller et al., 1991; Oslick et al., 1994; Zachos et al., 1999). However, the precision of estimates of the rate of change in $^{87}Sr/^{86}Sr$ is limited by the precision of the independent age model in marine records. Where age model control points are of low resolution or low certainty, changes in sedimentation rate may cause apparent variations in the rate of change in $^{87}Sr/^{86}Sr$ so that changes in the rate of $^{87}Sr/^{86}Sr$ cannot be confidently inferred. To date, available $^{87}Sr/^{86}Sr$ data for the Oligocene and early Miocene are derived from deep-sea sediment cores featuring only biostratigraphically derived age models, whose precision is limited by the biostratigraphic sampling resolution as well as the potential for diachroneity among events. Precision for such age models can be limited by long distances between examined biostratigraphic points in the core and the potential for diachroneity in the first occurrence or last occurrence of taxa in diverse locations, and may feature uncertainties from 0.5 to 4 million years (Miller et al., 1988). Over the last decade, astrochronology has emerged as a powerful independent chronometer, and the success of continuous coring and splicing of deep-ocean sediment cores has enabled the elaboration of precise independent age models based on orbital tuning of high-resolution benthic $\delta^{18}O$ records (Pälike et al., 2006; Liebrand et al., 2016; Westerhold et al., 2020; De Vleeschouwer et al., 2017).

In this study, we seek to apply the independent orbitally tuned Oligocene chronology for two purposes. First, we seek to evaluate the potential for dynamic changes in Sr sources by producing a $^{87}Sr/^{86}Sr$ record from a site with an independent orbitally resolved age model, Ocean Drilling Program (ODP) Site 1218 from the equatorial Pacific (Fig. 1), for which the original chronology (Pälike et al., 2006) was recently updated (Westerhold et al., 2020). The very rapid rate of change in seawater $^{87}Sr/^{86}Sr$ also provides the opportunity for improved age correlation among distal sites (Mcarthur et al., 2020). Therefore, our second objective is to improve the fidelity of the age model for two further sites which currently lack an orbitally resolved age model using existing reference curves and the Site 1218 record as an additional reference. For this objective, we focus on North Atlantic International Ocean Discovery Program Site 1406 (Newfoundland Margin) and Southern Ocean ODP Site 1168 (Tasman Rise), both emerging as important sites for Oligocene to early Miocene paleoceanographic studies (Scher et al., 2015; Hoem et al., 2022, 2021; Guitián and Stoll, 2021; Kim and Zhang, 2022; Egger et al., 2018; Liu et al., 2018; Spray et al., 2019; Boyle et al., 2017). At Site 1406, Sr isotope stratigraphy improves constraints on the duration of an early Miocene hiatus (van Peer et al., 2017b; Norris et al., 2014). The Oligocene to early Miocene Southern Ocean paleogeography produced strong provincialism in many marine taxa from Site 1168, so synchroneity with global biostratigraphic datums is uncertain. For paleoclimatic study, tuning to Site 1218 offers the advantage of providing a precise link with the complete benthic $\delta^{18}O$ record, therefore enabling direct correlation with the highest-resolution paleoclimatic record available for this time interval.

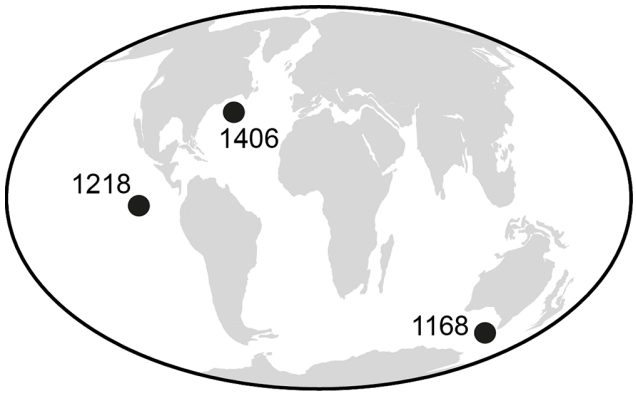

Figure 1. Location of ODP 1218, IODP 1406, and ODP 1168 with paleogeography during the Oligocene–Miocene transition. Reconstruction was made using the plate tectonic reconstruction service ODSN (http://www.odsn.de, last access: 11 December 2023).

2 Sites and methods

2.1 Sediments

Ocean Drilling Program (ODP) Leg 199, Site 1218 in the equatorial Pacific (8°53.378′ N, 135°22.00′ W; 4.8 km water depth) features a detailed astrochronologic age model from benthic $\delta^{18}O$ originally spanning 22 to 25 Ma (Pälike et al., 2006). Subsequently, continuous tuning at the precision of the 100 kyr eccentricity cycle from 21.81 Ma through the lowermost Oligocene was generated on the CENOGRID timescale (Westerhold et al., 2020). At Site 1218 we sought high resolution in the Middle Oligocene Glacial Interval (MOGI), previously hypothesized to feature inflection points in the $^{87}Sr/^{86}Sr$ curve (Oslick et al., 1994). We targeted samples between 59.93 and 211.94 revised meters of core depth (rmcd). Due to the modest carbonate content of Site 1218, not all targeted sample intervals contained sufficient foraminifera for analysis. We have picked > 2 mg of mixed species of planktonic or mixed species of benthic foraminifera, depending on the abundance in each sample. From some samples, populations of both benthic and planktic forams could be procured and we report the averaged $^{87}Sr/^{86}Sr$ ratio for the two populations.

Integrated Ocean Drilling Program (IODP) Expedition 342 recovered Paleogene to Neogene sedimentary sequences in contourite drift deposits off the coast of Newfoundland in the northwestern Atlantic. Here we focus on Site 1406 (40°21.0′ N, 51°39.0′ W; 3814 m b.s.l.) with samples dominantly from Hole A, but including a few samples from Holes B and C. The composite depth scale for the site (CCSF-A) is based on physical properties and trace element ratios from an XRF scanner (van Peer et al., 2017b) and is under revision as further benthic foraminifera and fine-fraction stable isotope data are produced. Consequently, where samples from all sites are plotted, we illustrate with the composite CCSF-A scale, but both depth scales are provided in data tables. Based on available biostratigraphy and previous age models (Norris et al., 2014; van Peer et al., 2017b), we sought samples spanning the age range 17 to 30 Ma, represented by depths from 23.9 to 200 m on the CCSF-A depth scale. In the Southern Hemisphere, ODP Site 1168 was drilled offshore of the Australian plate at the western margin of Tasmania at 43°36.57′ S, 139 144°24.76′ E and 2463 m water depth. This sequence is within a graben-developed basin with sediment accumulation since the latest Eocene (Exon et al., 2004). Based on available biostratigraphy (Stickley et al., 2004), we selected samples from Hole A, spanning the 16 to 27 Ma interval, representing sediments from 278 to 562 m depth on the meters below seafloor (m b.s.f.) depth scale used for ODP sites of this generation. Mixed planktonic foraminifera were picked for Sites 1406 and 1168.

2.2 Analytical

Strontium isotope ratios ($^{87}Sr/^{86}Sr$) were measured on ∼2 mg of cleaned foraminifera carbonates. Foraminifera samples were crushed open under binocular inspection, and the fragments were rinsed several times in Milli-Q water and methanol, then ultrasonicated to remove detrital contaminants (Pena et al., 2005). Each sample was treated individually to ensure that sufficient rinsing steps were applied. Cleaned fragments were dissolved in dilute double-distilled nitric acid, and the resulting solution was centrifuged at medium speed for 20 min to remove any potential detrital material left in the samples. The supernatant was transferred to clean Savillex-PFA beakers and Sr was chemically separated from sample matrix and interfering Rb using Triskem Sr-Spec resin through column chromatography procedures at the LIRA ultra-clean laboratory (Universitat de Barcelona).

Following sample purification, Sr isotope ratios were determined by multicollector inductively coupled mass spectrometry on a Nu Instruments (Wrexham, UK) Plasma 3 MC-ICPMS at the University of Barcelona (CciT-UB). For the determination of the $^{87}Sr/^{86}Sr$ isotope ratios, the contribution of ^{87}Rb to the ^{87}Sr signal was corrected from the measurement of the ^{85}Rb signal, assuming a $^{87}Sr/^{85}Sr$ ratio of 0.38562. The ^{86}Kr interference in ^{86}Sr, caused by impurities in the argon gas, was also corrected by measuring the ^{83}Kr signal and assuming a $^{83}Kr/^{86}Kr$ value of 0.66453. $^{87}Sr/^{86}Sr$ ratios were normalized for instrumental mass bias to $^{86}Sr/^{88}Sr = 0.1194$. Instrumental drift was corrected by sample-standard bracketing (SSB) using NBS987 = 0.710249 as the primary standard with matching standard and sample Sr concentrations. External analytical reproducibility during the session was ±0.000018 (2σ, $n = 19$). Procedural blanks are routinely measured during every analytical session. Typical procedural Sr blanks (including sample cleaning, purification, and analysis) are 369±264 pg, $n = 12$, and 1 σ. Blanks are systematically corrected for every measurement and the effect of the correction is in the sixth decimal place of the $^{87}Sr/^{86}Sr$ ratios, well below the external reproducibility of the analytical method (fifth decimal place). Values are normalized to SRM 987 using $^{86}Sr/^{86}Sr$ of 0.1194 and $^{87}Sr/^{86}Sr$ of 0.710249. This is identical to the normalization of (Mcarthur et al., 2020) using $^{87}Sr/^{86}Sr$ 0.709174 for modern marine Sr (EN-1 and similar), equivalent to 0.710248 for SRM (NIST) 987.

3 Results

Our new data from Site 1218 on the CENOGRID age model (Fig. 2, Table 1) reveal a similar long-term amplitude and rate of rise in $^{87}Sr/^{86}Sr$ as previously reported data on biostratigraphically constrained age models (Mcarthur et al., 2020). However, the new data reveal a 1 Myr duration of negligible $^{87}Sr/^{86}Sr$ rise (27–28 Ma) and local reversals in the overall trend of increasing $^{87}Sr/^{86}Sr$ during the Middle Oligocene Glacial Interval (MOGI) and at the Oligo-Miocene transition. The new data also reveal several intervals of an especially abrupt increase in $^{87}Sr/^{86}Sr$ within and at the end of the MOGI.

At Site U1406, a prominent reversal in the $^{87}Sr/^{86}Sr$ rise is observed between 48.7 and 45.4 m (Fig. 3a, depths described on the CCSF-A scale). A significant jump in $^{87}Sr/^{86}Sr$ suggests an appreciable hiatus between 33.3 and 34.7 m. The abrupt change in $^{87}Sr/^{86}Sr$ between 176.2 and 170.1 may also indicate a hiatus or significantly condensed interval. At Site 1168 (Fig. 3b), a prominent reversal in the $^{87}Sr/^{86}Sr$ rise occurs between 538.2 and 527.8 m b.s.f.

4 Discussion

4.1 Variation in the rate of change in $^{87}Sr/^{86}Sr$ at Site 1218

The steep long-term Oligocene to early Miocene increase in $^{87}Sr/^{86}Sr$ has long been recognized and variably attributed to exhumation of readily weathered radiogenic bedrock during the Himalayan orogeny (Krishnaswami et al., 1992; Raymo et al., 1988) or to accelerated weathering of radiogenic bedrock in Antarctica with the onset of its glaciation (Miller et al., 1991). The cause of this long-term increase is beyond the scope of this study and our focus is on the vari-

Table 1. ODP identifiers, CENOGRI age, and $^{87}Sr/^{86}Sr$ data for Site 1218.

Lab ID	Exp	Site	Hole	Core	Core type	Sect-ion	Section half	Top interval (cm)	Bottom interval (cm)	rmcd	Age CENOGRID	$^{87}Sr/^{86}Sr$	2 sigma analytical
B2	199	1218	B	7	H	1	W	125	130	59.93	18.73	0.708529	1.71×10^{-5}
B3	199	1218	B	7	H	3	W	75	80	62.43	19.10	0.708497	1.13×10^{-5}
A1	199	1218	A	7	H	3	W	50	55	67.29	19.67	0.708473	1.21×10^{-5}
A2	199	1218	A	7	H	5	W	50	55	70.29	20.12	0.708448	1.71×10^{-5}
B4	199	1218	B	8	H	3	W	100	105	73.29	20.66	0.708378	1.17×10^{-5}
B5	199	1218	B	9	H	3	W	32	37	82.07	21.50	0.708320	1.21×10^{-5}
B6	199	1218	B	9	H	5	W	105	110	85.45	21.82	0.708309	1.71×10^{-5}
A4	199	1218	A	9	H	4	W	82	87	90.32	22.37	0.708290	1.71×10^{-5}
A5	199	1218	A	9	H	6	W	20	25	92.67	22.65	0.708287	1.71×10^{-5}
B7	199	1218	B	10	H	3	W	82	87	94.54	22.90	0.708248	1.50×10^{-5}
B8	199	1218	B	10	H	4	W	87	92	96.12	23.03	0.708251	1.06×10^{-5}
B9	199	1218	B	10	H	5	W	141	146	98.17	23.17	0.708256	1.19×10^{-5}
B11	199	1218	B	11	H	3	W	147	150	107.26	24.06	0.708199	1.71×10^{-5}
B12	199	1218	B	12	H	3	W	107	112	118.18	24.95	0.708133	1.71×10^{-5}
B13	199	1218	B	13	H	6	W	17	22	131.57	26.03	0.708118	1.71×10^{-5}
1218A 14H1 15–25 cm	199	1218	A	14	H	1	W	15	25	138.00	26.46	0.708083	1.82×10^{-5}
A9	199	1218	A	14	H	1	W	100	105	138.73	26.52	0.708054	1.71×10^{-5}
1218A 14H2 115 cm	199	1219	A	15	H	2	W	115	117	140.27	26.64	0.708054	1.84×10^{-5}
A10	199	1218	A	14	H	3	W	80	85	141.59	26.74	0.708064	1.71×10^{-5}
1218B 15H1 35 cm	199	1218	B	15	H	1	W	35	38		27.04	0.708070	1.86×10^{-5}
B14	199	1218	B	15	H	2	W	30	35	147.04	27.10	0.708050	1.13×10^{-5}
B15	199	1218	B	15	H	4	W	80	85	150.56	27.34	0.708050	1.33×10^{-5}
1218B 16H1 25 cm	199	1218	B	16	H	1	W	25	26.5	156.17	27.71	0.708034	1.82×10^{-5}
B16	199	1218	B	16	H	1	W	70	75	156.63	27.75	0.708031	1.71×10^{-5}
B17	199	1218	B	16	H	2	W	107	112	158.55	27.91	0.708029	1.21×10^{-5}
B18	199	1218	B	16	H	5	W	60	65	162.03	28.15	0.708031	1.13×10^{-5}
C1	199	1218	C	10	H	2	W	100	105	164.77	28.42	0.708023	1.13×10^{-5}
1218C 10H3 5 cm	199	1218	C	10	H	3	W	5	7	165.25	28.45	0.708019	1.82×10^{-5}
B19	199	1218	B	17	H	3	W	120	125	170.40	28.65	0.707982	1.21×10^{-5}
1218C 11H1 115 cm	199	1218	C	11	H	1	W	115	117	173.77	28.91	0.708003	1.84×10^{-5}
C2	199	1218	C	11	H	2	W	130	135	175.45	29.03	0.707986	1.21×10^{-5}
B20	199	1218	B	18	H	5	W	10	15	182.15	29.43	0.708006	1.21×10^{-5}
A11	199	1218	A	18	H	4	W	37	45	185.68	29.66	0.707988	1.12×10^{-5}
A12	199	1218	A	19	H	2	W	67	75	192.20	30.14	0.707976	1.71×10^{-5}
1218C 12H6 85 cm	199	1218	C	12	X	6	W	85	87	191.63	30.17	0.707974	1.91×10^{-5}
B21	199	1218	B	20	X	3	W	117	122	199.97	30.73	0.707956	1.71×10^{-5}
B23	199	1218	B	21	X	4	W	12	17	211.94	31.55	0.707930	1.50×10^{-5}

ability in the rate of increase within the Oligocene to early Miocene.

Significantly, the precise independent chronology of Site 1218 confirms that the long-term Oligocene and early Miocene increase in $^{87}Sr/^{86}Sr$ is punctuated by significant structure, including reversals, periods of negligible $^{87}Sr/^{86}Sr$ increase, and more abrupt increases in $^{87}Sr/^{86}Sr$. Reversals beyond analytical uncertainty are also seen in published high-resolution mid-Oligocene $^{87}Sr/^{86}Sr$ records from both ODP Site 522 (Reilly et al., 2002) and ODP Site 689B (Mead and Hodell, 1995), suggesting that they are a robust feature of the Oligocene ocean Sr cycle. The uncertainty in absolute chronology complicates the inference of million-year-scale periods of stasis or abrupt $^{87}Sr/^{86}Sr$ increase in previously published records with biostratigraphic age models. To further evaluate how the rate of change in $^{87}Sr/^{86}Sr$ deviates from a monotonic increase from 32 to 18 Ma, we generate a smoothed fit to the data based on a local linear regression model (Fig. 4). In the model, local regressions were based on three to six consecutive samples and an age range of at least 0.25 Myr, with the exception of a single shorter span of only 0.18 Myr at 26 Ma. To estimate the rate of change, we illustrate the derivative of this smoothed fit, as well as the slope and its uncertainty, for each linear segment (Fig. 4b). This analysis illustrates periods of both a more rapid increase and a slowed $^{87}Sr/^{86}Sr$ increase or a decrease.

Table 2. $^{87}Sr/^{86}Sr$ data for Site U1406 and the assigned ages and age uncertainties.

Site	Hole	Core	Core type	Section	Section half	Top interval (cm)	Bottom interval (cm)	Depth CSF-A (m)	Depth CCSF-A (m)	$^{87}Sr/^{86}Sr$	Internal SE (2σ)	Midpoint age assigned (Ma)	Lower age (Ma)	Upper age (Ma)
1406	A	2	H	4	w	89	93	11.61	23.9	0.708625	0.000018	17.60	17.45	17.75
1406	A	2	H	5	w	36	40	12.58	24.9	0.708607	0.000018	17.82	17.67	17.97
1406	A	3	H	2	w	5	8	17.14	25.7	0.708582	0.000004	18.14	17.99	18.29
1406	A	3	H	4	w	89	92	20.98	29.6	0.708556	0.000004	18.43	18.28	18.58
1406	A	3	H	7	w	8	12	24.68	33.3	0.708556	0.000004	18.52	18.30	18.70
1406	A	4	H	1	w	139	143	26.61	34.7	0.708372	0.000004	20.66	20.29	20.91
1406	A	4	H	3	w	81	85	29.03	37.2	0.708350	0.000004	21.00	20.60	21.30
1406	A	5	H	2	w	6	9	36.27	45.4	0.708323	0.000003	21.30	20.90	21.60
1406	A	5	H	4	w	33	37	39.55	48.7	0.708341	0.000004	21.40	21.00	21.70
1406	A	6	H	6	w	74	80	52.47	63.0	0.708303	0.000004	22.20	21.80	22.50
1406	A	8	H	3	w	16	22	66.39	77.6	0.708267	0.000003	22.81	22.41	23.11
1406	C	8	H	1	w	80	84		80.3	0.708271	0.000014	22.90	22.50	23.20
1406	A	9	H	1	w	62	68	73.35	84.8	0.708252	0.000005	23.03	22.63	23.41
1406	A	9	H	6	w	91	95	81.16	92.6	0.708257	0.000004	23.15	22.75	23.53
1406	B	10	H	3	w	140	144		95.6	0.708249	0.000013	23.19	22.79	23.57
1406	B	10	H	5	w	70	74		97.9	0.708238	0.000013	23.32	22.92	23.69
1406	A	10	H	4	w	127	133	88.00	101.8	0.708208	0.000004	23.85	23.45	24.23
1406	A	11	H	3	w	53	59	95.26	109.2	0.708191	0.000004	24.16	23.76	24.54
1406	A	12	H	1	w	90	94	102.12	117.3	0.708161	0.000006	24.72	24.32	25.09
1406	A	12	H	6	w	44	48	109.16	124.4	0.708142	0.000007	25.07	24.67	25.52
1406	A	13	H	7	w	21	25	119.45	135.0	0.708126	0.000004	25.37	24.97	25.82
1406	A	14	H	4	w	97	103	125.70	141.8	0.708112	0.000007	25.64	25.24	26.09
1406	A	15	H	2	w	6	10	131.28	148.7	0.708097	0.000003	25.95	25.55	26.40
1406	A	15	H	5	w	103	107	136.81	154.3	0.708090	0.000004	26.10	25.70	26.55
1406	A	16	H	4	w	26	30	143.98	162.1	0.708074	0.000004	26.37	25.97	26.82
1406	A	16	H	6	w	66	70	147.38	165.5	0.708074	0.000005	26.52	26.12	26.97
1406	A	17	H	1	w	128	132	149.40	170.1	0.708068	0.000005	26.58	26.18	27.03
1406	A	17	H	4	w	86	90	153.48	174.2	0.708039	0.000003	27.31	26.71	28.21
1406	A	17	H	5	w	136	140	155.48	176.2	0.707999	0.000018	28.59	27.99	29.59
1406	A	18	H	1	w	19	23	157.51	184.7	0.707997	0.000018	28.68	28.08	29.68
1406	A	18	H	2	w	94	98	159.60	186.8	0.707984	0.000018	29.24	28.64	30.24
1406	A	18	H	4	w	20	24	161.86	189	0.707982	0.000004	29.33	28.73	30.33
1406	A	18	H	5	w	96	100	164.12	191	0.707976	0.000018	29.58	28.98	30.58
1406	A	19	H	2	w	15	19	166.37	200	0.707966	0.000018	29.97	29.37	30.97

Table 3. $^{87}Sr/^{86}Sr$ data for Site 1168 and the assigned ages and age uncertainties.

Site	Hole	Core	Core type	Section	Section half	Top interval (cm)	Bottom interval (cm)	Depth (m b.s.f.)	$^{87}Sr/^{86}Sr$	Internal SE (2σ)	Central age (Ma)	Min age (Ma)	Max age (Ma)
1168	A	30	X	5	W	2	8	278.25	0.708724	1.8×10^{-5}	16.29	16.14	16.44
1168	A	33	X	2	W	52	58	302.75	0.708549	1.8×10^{-5}	18.57	18.35	18.74
1168	A	37	X	1	W	43	49	339.26	0.708469	1.8×10^{-5}	19.67	19.39	19.87
1168	A	40	X	3	W	60	65	371.22	0.708394	1.8×10^{-5}	20.55	20.18	20.80
1168	A	41	X	1	W	5	8	377.36	0.708377	1.4×10^{-5}	21.02	20.62	21.32
1168	A	41	X	1	W	135	138	378.66	0.708363	1.3×10^{-5}	21.24	20.84	21.54
1168	A	41	X	6	W	34	37	385.15	0.708360	1.3×10^{-5}	21.28	20.88	21.58
1168	A	41	X	7	W	34	48	386.46	0.708372	1.4×10^{-5}	21.33	20.93	21.63
1168	A	42	X	3	W	45	26	390.78	0.708338	1.6×10^{-5}	21.63	21.23	21.93
1168	A	42	X	4	W	137	139	392.78	0.708287	1.8×10^{-5}	22.47	22.07	22.77
1168	A	43	X	5	W	55	57	403.06	0.708262	2.0×10^{-5}	22.90	22.50	23.28
1168	A	44	X	2	W	69	71	408.3	0.708284	2.0×10^{-5}	23.20	22.80	23.58
1168	A	45	X	3	W	143	145	420.14	0.708272	1.9×10^{-5}	23.30	22.90	23.68
1168	A	46	X	1	W	49	55	425.82	0.708230	1.8×10^{-5}	23.46	23.06	23.84
1168	A	48	X	4	W	65	68	449.65	0.708231	2.0×10^{-5}	23.70	23.30	24.08
1168	A	51	X	4	W	38	42	478.2	0.708192	1.8×10^{-5}	24.30	23.90	24.68
1168	A	55	X	5	W	33	39	518.06	0.708172	1.8×10^{-5}	24.51	24.11	24.96
1168	A	56	X	5	W	37	43	527.8	0.708129	1.8×10^{-5}	25.00	24.60	25.45
1168	A	57	X	5	W	113	117	538.25	0.708158	1.9×10^{-5}	25.20	24.80	25.65
1168	A	59	X	4	W	83	87	555.75	0.708057	2.2×10^{-5}	26.84	26.34	27.44
1168	A	60	X	2	W	57	61	562.09	0.708050	1.8×10^{-5}	27.02	26.52	27.62

At Site 1218, appreciably lower rates of $^{87}Sr/^{86}Sr$ increase (or even $^{87}Sr/^{86}Sr$ decrease) occur centered at 29 and 26.8 Ma during the MOGI and at 23 Ma during the OMT (Fig. 4). Each of these periods is followed by a large acceleration of $^{87}Sr/^{86}Sr$ increase. Our new data provide the most precise comparison between $^{87}Sr/^{86}Sr$ and the benthic $\delta^{18}O$ record of deep-sea temperature and ice volume because the records derive from the same deep-sea sediment archive (without correlation uncertainty) and the benthic $\delta^{18}O$ record is very high-resolution without aliasing, which can occur in records sampled at a resolution comparable to or greater than periods of orbital variation. The earliest slowing in the rate of $^{87}Sr/^{86}Sr$ increase and even decrease in $^{87}Sr/^{86}Sr$ which we resolve (centered at 29 Ma) coincides with the onset of heavier average benthic $\delta^{18}O$ demarcating the Middle Oligocene Glacial Interval (MOGI), and the recovery of rapid $^{87}Sr/^{86}Sr$ increase coincides with a shift towards more negative benthic $\delta^{18}O$ (ice volume decrease and/or deep-sea warming). The return to more intense glaciation from 28 to 26.8 Ma yields a decrease in $^{87}Sr/^{86}Sr$. The subsequent acceleration of $^{87}Sr/^{86}Sr$ increase at 26.5 Ma coincides with the onset of the negative shift in benthic $\delta^{18}O$ marking the end of the MOGI with ice volume decrease and/or deep-sea warming. The reduction of $^{87}Sr/^{86}Sr$ increase (or $^{87}Sr/^{86}Sr$ decrease) at the OMT coincides with an intense glacial phase and subsequently a consequent acceleration of $^{87}Sr/^{86}Sr$ increase at the end of the glacial phase. This event may coincide with the post-OMT acceleration previously defined as 22.4 Ma on the Cande and Kent (Cande and Kent, 1992) timescale (Oslick et al., 1994). We are unable to evaluate if there are similar < 0.5 Ma variations in the rate of $^{87}Sr/^{86}Sr$ change between 26 and 23 Ma as our sample resolution is not high enough in this interval. The main changes in slope are significant at the 68 % CI ($1\ \sigma$) level, but an increase in the sample resolution and number of data points would be needed to confidently distinguish many of these differences at the 95 % CI (2 sigma) level.

Variations in the isotopic composition of Sr inputs on timescales of 10^5 years are not expected to reflect changes in ocean crustal production rate and hydrothermal flux or significant changes in the composition of bedrock exposed on continents. Therefore, such changes are suggestive of change in either the intensity of continental weathering relative to hydrothermal sources or changes in the locus of the most intense continental weathering among continental sources of contrasting $^{87}Sr/^{86}Sr$. For example, a short-term relative increase in weathering intensity in areas underlain by younger average bedrock compared to older average bedrock would lead to a decreased $^{87}Sr/^{86}Sr$ of the riverine Sr flux and the marine reservoir. Alternatively, a short-term decrease in the intensity of weathering and thereby in the continental Sr flux (higher $^{87}Sr/^{86}Sr$ than the hydrothermal flux) could also lead to a decreased marine $^{87}Sr/^{86}Sr$. In either case, the long residence time of Sr in the ocean would result in lags between the onset of elevated fluxes and peak response in ocean chemistry and would cause significant attenuation of the time-varying input signal. An example of the phasing and amplitude variation in the $^{87}Sr/^{86}Sr$ of the Sr influx, which

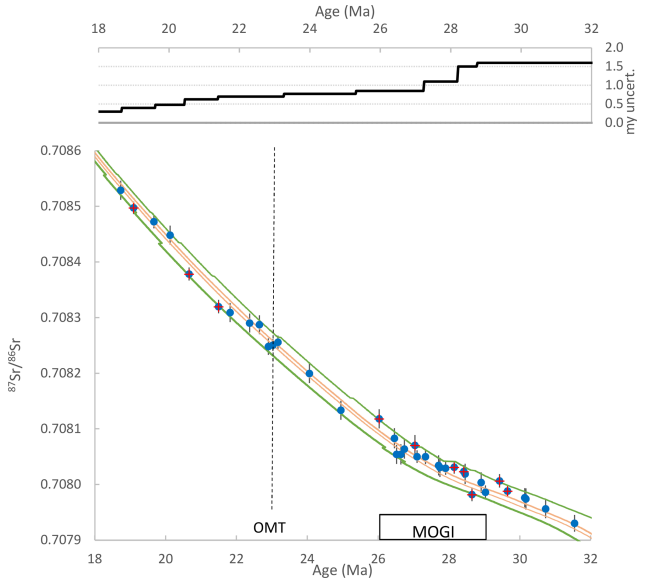

Figure 2. $^{87}Sr/^{86}Sr$ results from Site 1218 (blue circles with 2σ analytical uncertainty shown). The orange lines show the upper and lower bounds of the LOESS fit of biostratigraphically defined $^{87}Sr/^{86}Sr$ (Mcarthur et al., 2020). Samples falling outside the biostratigraphically defined long-term curve are highlighted in red. The green lines illustrate expanded age bounds for the LOESS fit of biostratigraphically constrained age models (Mcarthur et al., 2020). The upper panel illustrates the width of the age uncertainty of the expanded bounds. The Middle Oligocene Glacial Interval (MOGI) from 29 to 26 Ma is labeled, as is the Oligocene–Miocene transition (OMT). We highlight this duration of MOGI on the basis of the 1218 benthic $\delta^{18}O$ record as indicated in Fig. 4; it is slightly longer than the 28 to 26.3 Ma MOGI defined by Liebrand et al. (2016, 2017).

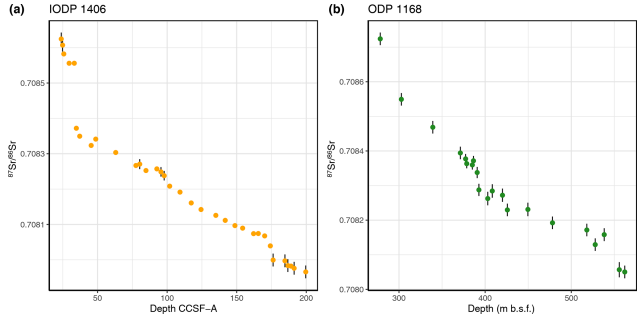

Figure 3. $^{87}Sr/^{86}Sr$ results from **(a)** U1406 and **(b)** 1168. Vertical error bars indicate 2σ analytical uncertainty where it exceeds the size of the plotted symbol.

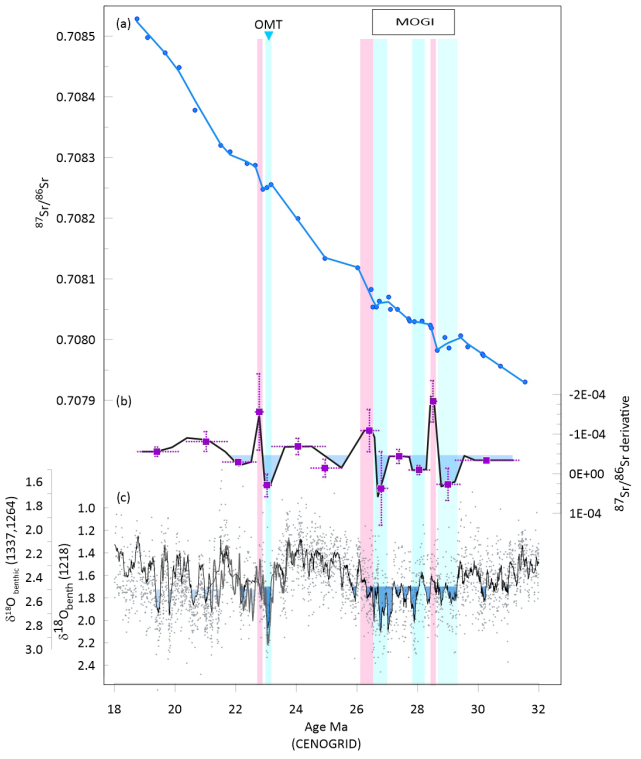

Figure 4. **(a)** Measured Site 1218 $^{87}Sr/^{86}Sr$ (symbols) and the smoothed fit from local linear regression (blue line). **(b)** The derivative of the smoothed fit (black line) and the slope of each linear segment (purple square), together with the uncertainty in the slope (vertical error bar, 68 % confidence interval) and the age range of the local linear fit (horizontal bar). Shading indicates sectors in which $^{87}Sr/^{86}Sr$ rises more slowly than the average rate over 32 to 18 Ma. **(c)** Benthic $\delta^{18}O$ measurements (gray points) and lines showing a 20-point running mean. Data from Site 1218 (black line from 21.46 to 32 Ma) (Pälike et al., 2006) and from the Cenozoic reference splice derived from U1337 (Holbourn et al., 2015) and ODP Site 1264 (Westerhold et al., 2020), both scaled as in Westerhold et al. (2020), are shown as a gray line from 21.2 to 24 Ma when overlapping with the 1219 record and a black line from 18 to 21.2 Ma. All data are plotted on the orbitally tuned CENOGRID timescale (Westerhold et al., 2020). Blue shading highlights intervals with benthic $\delta^{18}O$ more positive than 1.7‰ at Site 1218 and 2.5‰ in Cenozoic reference splice 1264 and U1337. The Middle Oligocene Glacial Interval (MOGI) from 29 to 26 Ma is labeled, as is the Oligocene–Miocene transition (OMT). Vertical blue and pink lines highlight intervals of slower and more rapid rates of change in $^{87}Sr/^{86}Sr$, respectively.

could yield the observed trends in marine $^{87}Sr/^{86}Sr$, is illustrated in Supplement Fig. S1 for a sample residence time of 2.5 Myr as suggested by Hodell et al. (1990). A shorter residence time has been proposed for the Oligocene by Paytan et al. (2021); for a shorter residence time, less extreme forcing would be required to simulate our observations. We caution that because the Sr isotopic system of the Oligocene to early Miocene is underconstrained, the observations of oceanic $^{87}Sr/^{86}Sr$ do not provide a unique solution for the variation in fluxes and/or their isotopic composition.

The coincidence of periods of slowed $^{87}Sr/^{86}Sr$ and the onset of glacial advance on Antarctica evidenced in benthic $\delta^{18}O$ suggests a climate control on the variations in the continental Sr flux on 10^5-year timescales from one or both of

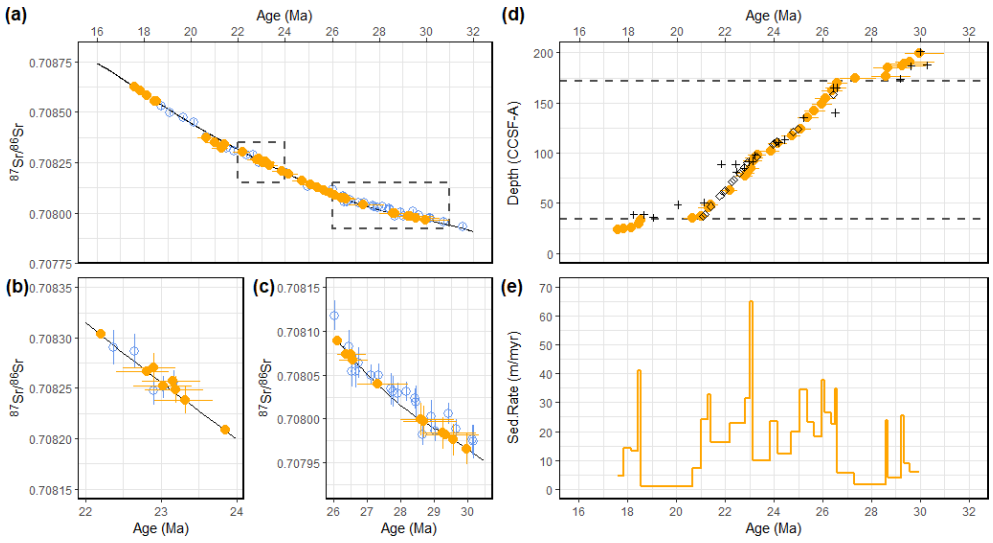

Figure 5. **(a)** Site U1406 $^{87}Sr/^{86}Sr$ data (orange) vs. the age (CENOGRID scale) assigned here; also shown are the new Site 1218 data (blue) and the Geological Time Scale (GTS) LOESS curve (Mcarthur et al., 2020). Panels **(b)** and **(c)** show insets. For Site U1406, horizontal lines indicate the uncertainty in the age assignments. **(d)** Age–depth plot for U1406A on the CCSF-A scale. Orange circles denote the ages from $^{87}Sr/^{86}Sr$ compared to previous biostratigraphy tie points (crosses; Norris et al., 2014) and magnetostratigraphy (open diamonds) (van Peer et al., 2017a). Horizontal dashed lines delimit the strongly condensed intervals; panel **(e)** shows the inferred sedimentation rate.

these mechanisms. Changes in the location of intense rainfall, such as a shift in the polar front or Intertropical Convergence Zone (ITCZ), could alter the locus of the most intense weathering. Potentially, episodes of Antarctic glacial expansion could cause an equatorward movement of the SH westerlies and associated rainfall band, or they could cause a mean ITCZ shift toward the Northern Hemisphere. However, climatically driven changes in the position of main heavy rainfall belts such as the ITCZ are usually limited to $< 10°$ latitude and may be longitudinally variable (Atwood et al., 2020). A movement of precipitation belts would have significant consequences for global riverine $^{87}Sr/^{86}Sr$ only in cases of fortuitous distribution of bedrock of widely different ages across the length scale of ITCZ movement. If a northward shift of the mean ITCZ significantly increased the Sr flux from a region of nonradiogenic Sr, the marine $^{87}Sr/^{86}Sr$ could experience a transient decrease. One potential such configuration could be the exposure of highly weatherable nonradiogenic rocks of the Deccan volcanic series of India and the Ethiopian Traps, located just north of the Equator in the late Oligocene (Kent and Muttoni, 2013).

It has also been proposed that glaciation can affect the weatherability of bedrock. Generally, the highest riverine dissolved Sr fluxes are produced from reactive young volcanic rock, as well as soluble carbonates, but the mechanical flouring of less reactive rock types by glacial erosion can significantly increase their weatherability and Sr contribution to the ocean. It has been suggested that weathering intensity of the Antarctic craton may have evolved over the late Eocene through Oligocene, as glacial flouring of Antarctic bedrock increased the weatherability of this continental Sr source (Miller et al., 1991; Oslick et al., 1994), contributing to the rise in ocean $^{87}Sr/^{86}Sr$. Intermittent glaciation, characterized by significant changes in the spatial extent of ice coverage, may alternately generate highly weatherable fine-grained silicates in a subglacial weathering-limited environment (low continental Sr fluxes) and then expose them to subaerial conditions of enhanced chemical weathering (high continental Sr flux). In previous biostratigraphic age models, apparent accelerations in the rate of $^{87}Sr/^{86}Sr$ increase at 32, 28, 22.4, 19.5, and 16.5 Ma (on the Cande and Kent timescale) occur 1 Myr after the deglaciation midpoint inferred from benthic $\delta^{18}O$ maxima in ODP 747 (Oslick et al., 1994). This was interpreted to result from deglacial exposure which may have contributed to a transient increase in the flux of radiogenic Sr to the ocean. With higher-resolution benthic $\delta^{18}O$ from 1218, we resolve more rapid responses of the $^{87}Sr/^{86}Sr$ ratio to several deglaciation phases.

East Antarctica is inferred to be underlain dominantly by Proterozoic and Archean bedrock (Kirkham et al., 1995). Exposed bedrock in East Antarctica is dominated by Archean and Proterozoic metamorphic rocks, with Paleozoic igneous and sedimentary rocks additionally exposed in the Transantarctic Mountains (Licht and Hemming, 2017). Although the Sr isotopic composition of bedrock in Antarctica can be measured directly only in current exposures in the Transantarctic Mountains and coastal areas, crustal rocks at the perimeters of major ice sheets may represent a major source of the sediment arriving at the margin and therefore be weatherable during retreat (Farmer et al., 2003). Because

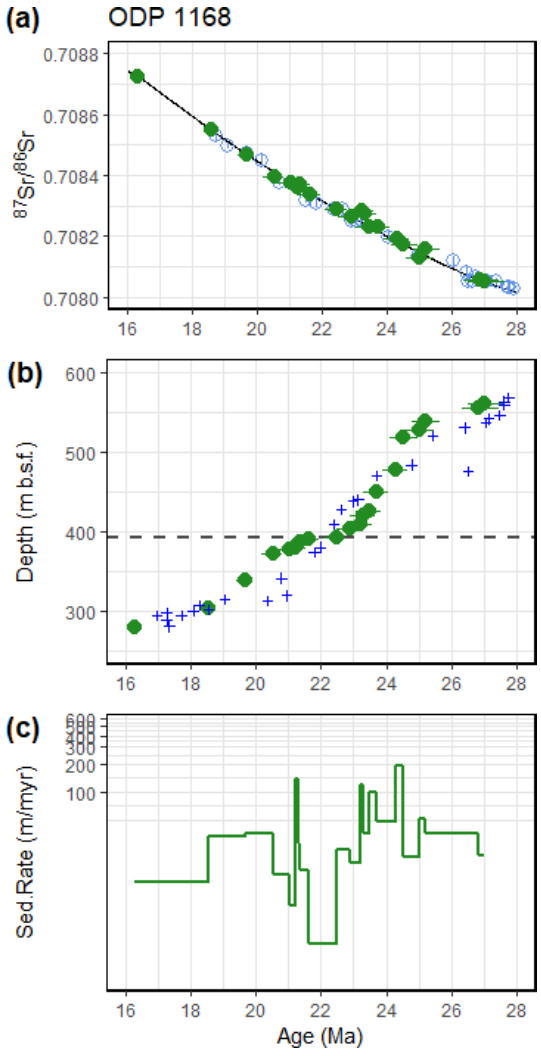

Figure 6. **(a)** Site 1168 $^{87}Sr/^{86}Sr$ data (green) vs. the age (CENOGRID scale) assigned here; also shown are the new Site 1218 data (blue open symbols) and the GTS LOESS curve (Mcarthur et al., 2020) **(b)**. Age–depth plot for Site 1168. Green diamonds denote the ages from $^{87}Sr/^{86}Sr$ compared to previous biostratigraphy-derived tie points (crosses). **(c)** Sedimentation rate implied by the $^{87}Sr/^{86}Sr$ age model. The horizontal dashed line in **(b)** highlights the period of significantly slowed sedimentation of the early Miocene.

erosion rates are highest at the perimeter of Antarctic Ice Sheet (Jamieson et al., 2010), the mapped bedrock in coastal areas may provide a reasonable representation of the source of sediment arriving at the glacial margin and being weatherable during retreat. Additionally, the fine-grained component of Last Glacial Maximum (LGM) tills exposed in the Ross Sea embayment provides constraints on the modern underlying composition of present erosion (Farmer et al., 2006). Present till composition includes very radiogenic compositions up to 0.740 attributed to erosion of the Neoproterozoic Beardsmore Formation and compositions in the range of 0.720 to 0.735 typical of 500 Ma Granite Harbor intrusive rocks exposed in the southern part of the Transantarctic Mountains as well as the Wilson terrane Proterozoic gneisses (Farmer et al., 2006). However, a caveat is that the currently exposed bedrock may be older than that exposed in the Oligocene due to denudation, and younger, less radiogenic bedrock may have contributed more to glacial flouring in the Oligocene, making global fluxes less sensitive to the Antarctic weathering regime.

4.2 Sr isotope constraints on age models of Site U1406 and Site 1168

Previous approaches for Sr isotope stratigraphy for the Cenozoic have inferred a continuous rise in $^{87}Sr/^{86}Sr$. The data from Site 1218 suggest several intervals with a negligible rate of rise and/or reversals. In the interval from 28 to 30 Ma, five of our nine samples feature $^{87}Sr/^{86}Sr$ ratios whose analytical 95 % CIs fall outside the bounds of the reference $^{87}Sr/^{86}Sr$ curve of that age generated from biostratigraphically constrained age models (Mcarthur et al., 2020). For these intervals, particularly during the MOGI, age assignments from Sr isotope stratigraphy have a higher uncertainty than previously inferred. In the interval from 28 to 30 Ma, the deviation between the CENOGRID age and the reference curve ranges from 1.1 Myr older than the reference curve to 0.7 Myr younger, a significantly wider uncertainty than the ±120 to 180 kyr uncertainty predicted for the reference curve. In the early Miocene, between 21.7 and 19.4 Ma, a number of our Site 1218 CENOGRID ages also deviate from the ages from the reference curve by 0.18 to 0.42 Myr, which is greater uncertainty than the ±70 to 50 kyr reported for the reference curve. Consequently, in deriving ages for Site U1406 and Site 1168 on the CENOGRID scale from $^{87}Sr/^{86}Sr$, we expand the bounds of the age uncertainties from Mcarthur et al. (2020) to encompass the Site 1218 data (Fig. 2, green bounds). The width of the resulting age uncertainty therefore ranges from 300 kyr in the early Miocene to 1.6 Myr in the early to middle Oligocene.

In addition to these greater uncertainties, stratigraphic constraints prohibit reversals in ages where there is no independent evidence for reworking or sediment disturbance. Our Site 1218 data indicate that reversals in $^{87}Sr/^{86}Sr$ are certain within the time interval of 29–26 Ma and likely at the OMT. Thus, in estimating ages for 1168 and U1406 based on $^{87}Sr/^{86}Sr$, we assign an initial age based on Mcarthur et al. (2020) but adjust the age to preserve stratigraphic relationships (e.g., no age reversals in our age assignments). The detailed age models are shown in Tables 2 and 3.

4.2.1 Site U1406

A condensed interval and hiatus have been recognized in the Oligocene to early Miocene sediments of U1406 on the basis of bio- and magnetostratigraphy (Fig. 5) (Norris et al.,

2014; van Peer et al., 2017a). Because of the slow rate of the Site U1406 $^{87}Sr/^{86}Sr$ change and reversals during the MOGI, the U1406 $^{87}Sr/^{86}Sr$ cannot precisely pinpoint the duration of the hiatus or condensed interval between 170.1 and 174.2 m (CCSF-A) (Fig. 5). The condensed interval could contain 2 Myr (28.45 to 26.58 Ma) or < 1 Myr (27.3 to 26.58 Ma). On the other hand, the early Miocene condensed interval between 34.7 and 33.3 m (CCSF-A) is constrained to represent 2 Myr. Sustained high sedimentation rates are confirmed between 21 and 26 Ma. Between 26.4 and 21 Ma, the $^{87}Sr/^{86}Sr$ age model is in close agreement with that devised from magnetostratigraphy (Van Peer et al., 2017a). The Site 1406 $^{87}Sr/^{86}Sr$ data indicate that the uppermost 25 m of sediment in U1406, which is difficult to date due to sparse biostratigraphic markers, was likely deposited between 18.5 and 17.6 Ma.

4.2.2 Site 1168

This first $^{87}Sr/^{86}Sr$ stratigraphy for Site 1168 implies significant differences in inferred ages compared to existing biostratigraphy, including significantly higher sedimentation rates in the early Miocene (20.5 to 18.5 Ma), but comparably slower sedimentation rates between 21.6 and 22.5 Ma just after the OMT (Fig. 6). This is slightly earlier than the early Miocene hiatus found in many deep-sea sedimentary records between 19 and 20 Ma; however, in other deep-sea records the precise timing of early Miocene depositional gaps is not yet resolved and could coincide with the condensed interval in 1168 (Sibert and Rubin, 2021). Age assignments remain less precise in the middle Oligocene (25 to 27 Ma) due to the low rate of change and reversals in $^{87}Sr/^{86}Sr$ during this time interval, as well as the current low $^{87}Sr/^{86}Sr$ sample coverage.

5 Conclusions

The $^{87}Sr/^{86}Sr$ record from the astrochronologically dated Site 1218 provides the opportunity to assess ∼ 1 Myr variations in the Sr flux to the ocean during a period of dynamic Antarctic cryosphere evolution. Our dataset resolves relationships between the locus and/or intensity of continental weathering and phases of Antarctic glaciation. Overall, the data suggest that the major changes in mid-Oligocene high-latitude climate – particularly the onset and end of the MOGI – do exhibit a close coupling between seawater $^{87}Sr/^{86}Sr$ and benthic $\delta^{18}O$. During periods of expanded ice coverage on Antarctica such as the MOGI, then, our data are consistent with either northward shifts in the ITCZ precipitation to areas of nonradiogenic bedrock and/or lowered weathering fluxes from highly radiogenic glacial flours on Antarctic. Future higher-resolution sampling is required to further evaluate the significance of such changes. Additionally, the new $^{87}Sr/^{86}Sr$ record from Sites 1168 and U1406 improves the precision of age correlation of these Northern Hemisphere and Southern Hemisphere midlatitude sites with each other and with high-resolution benthic $\delta^{18}O$ records aligned with the CENOGRID chronology.

Data availability. All data presented in this study are available in Tables 1–3.

Supplement. The supplement related to this article is available online at: https://doi.org/10.5194/cp-20-25-2024-supplement.

Author contributions. The study was conceived by HMS. Samples were selected by HMS with advice from HP. Foraminifera were prepared by JG, IHA, and TT. Sr isotope analyses were completed by LDP. Interpretation was completed by HMS, and figures were prepared by HMS and JG. The paper was written by HMS with input from all authors.

Competing interests. The contact author has declared that none of the authors has any competing interests.

Disclaimer. Publisher's note: Copernicus Publications remains neutral with regard to jurisdictional claims made in the text, published maps, institutional affiliations, or any other geographical representation in this paper. While Copernicus Publications makes every effort to include appropriate place names, the final responsibility lies with the authors.

Acknowledgements. We thank Romain Alosius for assistance picking foraminifera and Laura Arnold for initial evaluation of foraminifera preservation. We gratefully acknowledge the Ocean Drilling Program and International Ocean Discovery Program for providing the samples used in this study.

Financial support. This research has been supported by the Schweizerischer Nationalfonds zur Förderung der Wissenschaftlichen Forschung (grant no. 200021_182070).

Review statement. This paper was edited by Alberto Reyes and reviewed by one anonymous referee.

References

Atwood, A. R., Donohoe, A., Battisti, D. S., Liu, X., and Pausata, F. S.: Robust longitudinally variable responses of the ITCZ to a myriad of climate forcings, Geophys. Res. Lett., 47, e2020GL088833, https://doi.org/10.1029/2020GL088833, 2020.

Boyle, P. R., Romans, B. W., Tucholke, B. E., Norris, R. D., Swift, S. A., and Sexton, P. F.: Cenozoic North Atlantic deep circulation history recorded in contourite drifts,

offshore Newfoundland, Canada, Mar. Geol., 385, 185–203, https://doi.org/10.1016/j.margeo.2016.12.014, 2017.

Cande, S. C. and Kent, D. V.: A new geomagnetic polarity time scale for the Late Cretaceous and Cenozoic, J. Geophys. Res.-Solid Earth, 97, 13917–13951, https://doi.org/10.1029/92JB01202, 1992.

De Vleeschouwer, D., Vahlenkamp, M., Crucifix, M., and Pälike, H.: Alternating Southern and Northern Hemisphere climate response to astronomical forcing during the past 35 my, Geology, 45, 375–378, https://doi.org/10.1130/G38663.1, 2017.

Egger, L. M., Bahr, A., Friedrich, O., Wilson, P. A., Norris, R. D., van Peer, T. E., Lippert, P. C., Liebrand, D., and Pross, J.: Sea-level and surface-water change in the western North Atlantic across the Oligocene–Miocene Transition: a palynological perspective from IODP Site U1406 (Newfoundland margin), Mar. Micropaleontol., 139, 57–71, https://doi.org/10.1016/j.marmicro.2017.11.003, 2018.

Exon, N. F., Kennett, J. P., and Malone, M. J.: Leg 189 synthesis: Cretaceous–Holocene history of the Tasmanian gateway, Proceedings of the ocean drilling program, Scientific Results, 189, 1–37, https://doi.org/10.2973/odp.proc.sr.189.101.2004,

Farmer, G. L., Barber, D., and Andrews, J.: Provenance of Late Quaternary ice-proximal sediments in the North Atlantic: Nd, Sr and Pb isotopic evidence, Earth Planet. Sci. Lett., 209, 227–243, https://doi.org/10.1016/S0012-821X(03)00068-2, 2003.

Farmer, G. L., Licht, K., Swope, R. J., and Andrews, J.: Isotopic constraints on the provenance of fine-grained sediment in LGM tills from the Ross Embayment, Antarctica, Earth Planet. Sci. Lett., 249, 90–107, https://doi.org/10.1016/j.epsl.2006.06.044, 2006.

Galy, A., France-Lanord, C., and Derry, L. A.: The Late Oligocene-Early Miocene Himalayan belt constraints deduced from isotopic compositions of Early Miocene turbidites in the Bengal Fan, Tectonophysics, 260, 109–118, 1996.

Guitián, J. and Stoll, H. M.: Evolution of Sea Surface Temperature in the Southern Mid-latitudes from Late Oligocene through Early Miocene, Paleoceanogr. Paleoclimatol., 36, e2020PA004199, https://doi.org/10.1029/2020PA004199, 2021.

Hodell, D. A., Mead, G. A., and Mueller, P. A.: Variation in the strontium isotopic composition of seawater (8 Ma to present): Implications for chemical weathering rates and dissolved fluxes to the oceans, Chem. Geol.: Isotope Geoscience section, 80, 291–307, 1990.

Hoem, F. S., Sauermilch, I., Hou, S., Brinkhuis, H., Sangiorgi, F., and Bijl, P. K.: Late Eocene–early Miocene evolution of the southern Australian subtropical front: a marine palynological approach, J. Micropalaeontol., 40, 175–193, https://doi.org/10.5194/jm-40-175-2021, 2021, 2021.

Hoem, F. S., Sauermilch, I., Aleksinski, A. K., Huber, M., Peterse, F., Sangiorgi, F., and Bijl, P. K.: Strength and variability of the Oligocene Southern Ocean surface temperature gradient, Communication. Earth Environ., 3, 322, https://doi.org/10.1038/s43247-022-00666-5, 2022.

Holbourn, A., Kuhnt, W., Kochhann, K. G., Andersen, N., and Sebastian Meier, K.: Global perturbation of the carbon cycle at the onset of the Miocene Climatic Optimum, Geology, 43, 123–126, https://doi.org/10.1130/G36317.1, 2015.

Jamieson, S. S., Sugden, D. E., and Hulton, N. R.: The evolution of the subglacial landscape of Antarctica, Earth Planet. Sci. Lett., 293, 1–27, https://doi.org/10.1016/j.epsl.2010.02.012, 2010.

Kent, D. V. and Muttoni, G.: Modulation of Late Cretaceous and Cenozoic climate by variable drawdown of atmospheric pCO2 from weathering of basaltic provinces on continents drifting through the equatorial humid belt, Clim. Past, 9, 525–546, https://doi.org/10.5194/cp-9-525-2013, 2013.

Kim, B. and Zhang, Y. G.: Methane hydrate dissociation across the Oligocene–Miocene boundary, Nat. Geosci., 15, 203-209, https://doi.org/10.1038/s41561-022-00895-5, 2022.

Kirkham, R., Chorlton, L., and Carriere, J.: Generalized geology of the world, Generalized geological map of the world and linked databases. Geological Survey of Canada, Open File 2915d, https://doi.org/10.4095/195143, 1995.

Krishnaswami, S., Trivedi, J., Sarin, M., Ramesh, R., and Sharma, K.: Strontium isotopes and rubidium in the Ganga-Brahmaputra river system: Weathering in the Himalaya, fluxes to the Bay of Bengal and contributions to the evolution of oceanic87Sr/86Sr, Earth Planet. Sci. Lett., 109, 243–253, https://doi.org/10.1016/0012-821X(92)90087-C, 1992.

Licht, K. J. and Hemming, S. R.: Analysis of Antarctic glacigenic sediment provenance through geochemical and petrologic applications, Quaternary Sci. Rev., 164, 1–24, https://doi.org/10.1016/j.quascirev.2017.03.009, 2017.

Liebrand, D., Beddow, H. M., Lourens, L. J., Pälike, H., Raffi, I., Bohaty, S. M., Hilgen, F. J., Saes, M. J., Wilson, P. A., and van Dijk, A. E.: Cyclostratigraphy and eccentricity tuning of the early Oligocene through early Miocene (30.1–17.1 Ma): Cibicides mundulus stable oxygen and carbon isotope records from Walvis Ridge Site 1264, Earth Planet. Sci. Lett., 450, 392–405, https://doi.org/10.1016/j.epsl.2016.06.007, 2016.

Liebrand, D., de Bakker, A. T., Beddow, H. M., Wilson, P. A., Bohaty, S. M., Ruessink, G., Pälike, H., Batenburg, S. J., Hilgen, F. J., and Hodell, D. A.: Evolution of the early Antarctic ice ages, P. Natl. Acad. Sci. USA, 114, 3867–3872, 2017.

Liu, Z., He, Y., Jiang, Y., Wang, H., Liu, W., Bohaty, S. M., and Wilson, P. A.: Transient temperature asymmetry between hemispheres in the Palaeogene Atlantic Ocean, Nat. Geosci., 11, 656–660, https://doi.org/10.1038/s41561-018-0182-9, 2018.

McArthur, J., Howarth, R., Shields, G., and Zhou, Y.: Strontium isotope stratigraphy, in: Geologic time scale 2020, Elsevier, 211–238, https://doi.org/10.1016/B978-0-12-824360-2.00007-3, 2020.

Mead, G. A. and Hodell, D. A.: Controls on the 87Sr/86Sr composition of seawater from the middle Eocene to Oligocene: Hole 689B, Maud Rise, Antarctica, Paleoceanography, 10, 327–346, https://doi.org/10.1029/94PA03069, 1995.

Miller, K. G., Feigenson, M. D., Kent, D. V., and Olsson, R. K.: Upper Eocene to Oligocene isotope (87Sr/86Sr, δ18O, δ13C) standard section, Deep sea drilling Project site 522, Paleoceanography, 3, 223–233, https://doi.org/10.1029/PA003i002p00223, 1988.

Miller, K. G., Feigenson, M. D., Wright, J. D., and Clement, B. M.: Miocene isotope reference section, Deep Sea Drilling Project Site 608: an evaluation of isotope and biostratigraphic resolution, Paleoceanography, 6, 33–52, https://doi.org/10.1029/90PA01941, 1991.

Myrow, P. M., Hughes, N. C., Derry, L. A., McKenzie, N. R., Jiang, G., Webb, A. A. G., Banerjee, D. M., Paulsen, T. S., and Singh, B. P.: Neogene marine isotopic evolution and the erosion of Lesser Himalayan strata: Implications for Cenozoic tectonic history, Earth Planet. Sci. Lett., 417, 142–150, 2015.

Norris, R., Wilson, P., and Blum, P.: Proceedings of the Integrated Ocean Drilling Program Exp. 342, College Station, TX: Integrated Ocean Drilling Program, https://doi.org/10.2204/iodp.proc.342.107.2014, 2014.

Oslick, J. S., Miller, K. G., Feigenson, M. D., and Wright, J. D.: Oligocene-Miocene strontium isotopes: Stratigraphic revisions and correlations to an inferred glacioeustatic record, Paleoceanography, 9, 427–443, https://doi.org/10.1029/94PA00249, 1994.

Pälike, H., Norris, R. D., Herrle, J. O., Wilson, P. A., Coxall, H. K., Lear, C. H., Shackleton, N. J., Tripati, A. K., and Wade, B. S.: The heartbeat of the Oligocene climate system, Science, 314, 1894–1898, https://doi.org/10.1126/science.1133822, 2006.

Palmer, M. and Elderfield, H.: Sr isotope composition of sea water over the past 75 Myr, Nature, 314, 526–528, https://doi.org/10.1038/314526a0, 1985.

Paytan, A., Griffith, E. M., Eisenhauer, A., Hain, M. P., Wallmann, K., and Ridgwell, A.: A 35-million-year record of seawater stable Sr isotopes reveals a fluctuating global carbon cycle, Science, 371, 1346–1350, 2021.

Pena, L., Calvo, E., Cacho, I., Eggins, S., and Pelejero, C.: Identification and removal of Mn-Mg-rich contaminant phases on foraminiferal tests: Implications for Mg/Ca past temperature reconstructions, Geochem. Geophys. Geosyst., 6, 1–25, https://doi.org/10.1029/2005GC000930, 2005.

Peucker-Ehrenbrink, B. and Fiske, G. J.: A continental perspective of the seawater 87Sr/86Sr record: a review, Chem. Geol., 510, 140–165, https://doi.org/10.1016/j.chemgeo.2019.01.017, 2019.

Raymo, M. E., Ruddiman, W. F., and Froelich, P. N.: Influence of late Cenozoic mountain building on ocean geochemical cycles, Geology, 16, 649–653, https://doi.org/10.1130/0091-7613(1988)016<0649:IOLCMB>2.3.CO;2, 1988.

Reilly, T. J., Miller, K. G., and Feigenson, M. D.: Latest Eocene-earliest Miocene Sr isotopic reference section, Site 522, eastern South Atlantic, Paleoceanography, 17, 18-11–18-19, https://doi.org/10.1029/2001PA000745, 2002.

Scher, H. D., Whittaker, J. M., Williams, S. E., Latimer, J. C., Kordesch, W. E., and Delaney, M. L.: Onset of Antarctic Circumpolar Current 30 million years ago as Tasmanian Gateway aligned with westerlies, Nature, 523, 580–583, https://doi.org/10.1038/nature14598, 2015.

Sibert, E. C. and Rubin, L. D.: An early Miocene extinction in pelagic sharks, Science, 372, 1105–1107, https://doi.org/10.1126/science.aaz3549, 2021.

Spray, J. F., Bohaty, S. M., Davies, A., Bailey, I., Romans, B. W., Cooper, M. J., Milton, J. A., and Wilson, P. A.: North Atlantic evidence for a unipolar icehouse climate state at the Eocene-Oligocene Transition, Paleoceanogr. Paleoclimatol., 34, 1124–1138, https://doi.org/10.1029/2019PA003563, 2019.

Stickley, C., Brinkhuis, H., McGonigal, K., Chaproniere, G., Fuller, M., Kelly, D., Nürnberg, D., Pfuhl, H., Schellenberg, S., and Schönfeld, J.: Late Cretaceous–Quaternary biomagnetostratigraphy of ODP Sites 1168, 1170, 1171, and 1172, Tasmanian Gateway, Proceedings of the Ocean Drilling Program, Sci. Res., 189, 1–57, https://doi.org/10.2973/odp.proc.sr.189.111.2004,

van Peer, T. E., Xuan, C., Lippert, P. C., Liebrand, D., Agnini, C., and Wilson, P. A.: Extracting a detailed magnetostratigraphy from weakly magnetized, Oligocene to early Miocene sediment drifts recovered at IODP Site U1406 (Newfoundland margin, northwest Atlantic Ocean), Geochem. Geophys. Geosyst., 18, 3910–3928, https://doi.org/10.1002/2017GC007185, 2017a.

van Peer, T. E., Liebrand, D., Xuan, C., Lippert, P. C., Agnini, C., Blum, N., Blum, P., Bohaty, S. M., Bown, P., and Greenop, R.: Data report: revised composite depth scale and splice for IODP Site U1406, https://doi.org/10.2204/iodp.proc.342.202.2017, 2017b.

Westerhold, T., Marwan, N., Drury, A. J., Liebrand, D., Agnini, C., Anagnostou, E., Barnet, J. S., Bohaty, S. M., De Vleeschouwer, D., and Florindo, F.: An astronomically dated record of Earth's climate and its predictability over the last 66 million years, Science, 369, 1383–1387, https://doi.org/10.1126/science.aba685, 2020.

Yang, Y., Galy, A., Yang, R., Liu, Y., Zhang, W., Ruan, X., Fang, X., Jin, Z., Song, B., and Yan, M.: Intense metamorphism-generated radiogenic Sr regulated Cenozoic water Sr isotope evolution on the NE Tibetan Plateau: A perspective on Qilian orogen denudation and Asian eolian transport, Geol. Soc. Am. Bull., 165, 2237–2254, https://doi.org/10.1130/B36525.1, 2022.

Zachos, J. C., Opdyke, B. N., Quinn, T. M., Jones, C. E., and Halliday, A. N.: Early Cenozoic glaciation, Antarctic weathering, and seawater 87Sr/86Sr: Is there a link?, Chem. Geol., 161, 165–180, https://doi.org/10.1016/S0009-2541(99)00085-6, 1999.